IOP Publishing Phys. Med. Biol. 65 (2020) 065007 https://doi.org/10.1088/1361-6560/ab7686

Physics in Medicine & Biology

IPEM Institute of Physics and Engineering in Medicine

PAPER

Stylized versus voxel phantoms: a juxtaposition of organ depth distributions

Keith T Griffin[1], **Thomas A Cuthbert**[1,2], **Shaheen A Dewji**[2] **and Choonsik Lee**[1]

[1] Division of Cancer Epidemiology and Genetics, National Cancer Institute, National Institutes of Health, Rockville, MD, United States of America

[2] Department of Nuclear Engineering, College of Engineering, Texas A&M University, College Station, TX, United States of America

E-mail: choonsik.lee@nih.gov

RECEIVED
2 August 2019

REVISED
31 January 2020

ACCEPTED FOR PUBLICATION
14 February 2020

PUBLISHED
20 March 2020

Keywords: organ depth, anthropomorphic phantoms, stylized phantoms, voxel phantoms, depth distribution, organ position

Supplementary material for this article is available online

Abstract

For external irradiation, the variability in organ dose estimation found between computational phantom generations arises particularly from the differences in organ positioning. This work represents the first effort to quantify the differences in organ depth below the body surface between a stylized and voxel phantom series. Herein, the revised Oak Ridge National Laboratory stylized phantom series and the University of Florida/National Cancer Institute voxel phantom series were compared. Both series include whole-body models of the newborn; the 1-, 5-, 10-, and 15-year-old; and the adult human. Organ depths from eight different directions applicable to external irradiation geometries were computed: antero-posterior, postero-anterior, left and right lateral, rotational, isotropic, cranial and caudal directions. Organ depths in the stylized phantoms were computed using a ray-tracing technique available through Monte Carlo radiation transport simulations in MCNP6. Organ depths in the voxel phantom were found using phantom matrix manipulation. Resultant organ depths for both series were plotted as distributions; available are twenty-four organs and two bone tissue distributions for each of six phantom ages and in each of the eight directional geometries. Quantitative data descriptors (e.g. mean and median depths) were also tabulated. For demonstration purposes, a literature review of relevant stylized versus voxel comparison works was performed to explore where the quantification of organ depth differences can provide further insight or evidence to study conclusions. The entire dataset of organ depth distributions and their data descriptors can be found in online supplementary files.

1. Introduction

With the exponential growth in computing speed and power over the past several decades, realism in computational models of the human body, termed anthropomorphic phantoms, has evolved (Xu 2014). While the first generation of phantoms was defined through simple geometrical surfaces, the second generation of phantoms was based on data sourced from segmented computed tomographic medical images; these phantoms have accordingly been termed the mathematical (stylized) generation and voxel generation, respectively. Shortcomings of the voxel phantom generation, such as its rigidity and inability to be modified to match the body type of another person, have led to the development of the third and latest phantom type known as the hybrid phantom generation. Hybrid phantoms are represented through polygonal meshes within modern computer aided design software and capture the best qualities of previous phantom generations: anatomical realism and flexibility; these phantoms can be converted to a voxel phantom format as necessary for use in radiation transport codes (Lee *et al* 2007).

New phantoms are being developed at an increasing pace (Zaidi and Xu 2007, Xu 2014, Xie *et al* 2018, 2019, Xie and Zaidi 2019) to better represent the individualized anatomy, which can strongly influence organ dosimetry estimations. However, many U.S. and international agencies continue to use the first generation of

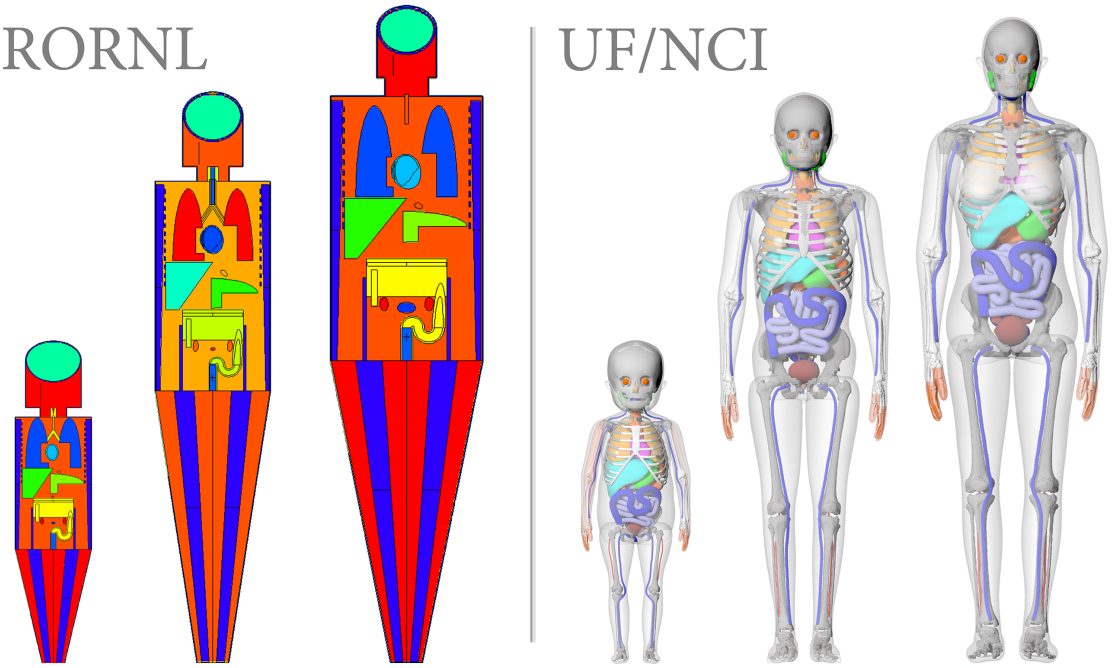

Figure 1. Frontal views of the RORNL series (left) and female members of the UF/NCI series (right). From left to right, three out of the six phantoms ages within each series are visualized: the 1-year-old, 10-year-old, and adult.

stylized phantoms for their modelling needs in radiation protection estimations or dose reconstruction, such as the Environmental Protection Agency (Eckerman and Ryman 1993, 2016b, Bellamy *et al* 2018, Veinot *et al* 2017), U.S. Nuclear Regulatory Commission (2015a, 2015b, Dewji *et al* 2017), and Radiation Effects Research Foundation (Roesch 1987, Young and Kerr 2005). New phantoms provide higher-fidelity anatomy, allowing for improved individualized dosimetry; however, there may be certain cases, such as whole-body exposures to penetrating radiations, where stylized phantoms can provide nearly identical results (Bellamy *et al* 2016a, Hiller and Dewji 2017). It has therefore been the scope of many studies to determine if the dosimetric consequences expected from a transition to newer generations of phantoms are beneficial to specific applications. Often in the literature, the dosimetric differences seen between the two generations of phantoms are explained through visual means of cross-sectional image comparisons to show differences in organ positioning (Bellamy *et al* 2016a, Yoriyaz *et al* 2000, Lee and Lee 2004, 2007, Liu *et al* 2010).

In the present work, an underlying knowledge gap is explored—a quantification of body shielding differences between stylized and voxel phantoms for internal organs. Methodology will be described that allows the distance from the body surface to an organ to be calculated from any directional exposure; these distances are calculated from random points sampled within each organ and plotted as a depth distribution. The application of these organ depth distributions can help interpret the phantom dosimetry simulation results in external radiation protection or other phantom modelling scenarios.

2. Background

This work will consider the stylized phantom series developed at Oak Ridge National Laboratory (ORNL), which was later revised by Han *et al* to reflect changes in both organ elemental composition and positioning (Cristy and Eckerman 1987, Han *et al* 2006). This revised ORNL (RORNL) phantom series, depicted in figure 1, is defined for use within the Monte Carlo N-Particle transport code (MCNP) as a series of implicit surface equations (Han *et al* 2006). Boolean operators are used with the surface equations to define the physical space occupied by each organ. The series is composed of six ages, representing the newborn, 1-, 5-, 10-, 15-year-old, and the adult. The RORNL phantoms are hermaphrodites, such that the sex-specific organs are combined into one model.

The RORNL phantom series, representing one such stylized phantom series still in use by radiation protection agencies, will be compared against the University of Florida/National Cancer Institute (UF/NCI) voxel phantom series, representing a newly developed phantom series (Lee *et al* 2010). The UF/NCI phantom series was originally created in hybrid format. Prior work used an in-house voxelization code to convert these hybrid phantoms into voxel format for use in Monte Carlo codes; the voxel dimensions for these converted

UF/NCI phantoms are detailed in prior work by the phantom developers (Lee *et al* 2010). The UF/NCI series is composed of twelve members, with the same ages as the RORNL series but with sex distinction.

Differences in organ depth distributions will be determined for external exposure scenarios as described by Publication 116 of the International Commission on Radiological Protection (ICRP) (ICRP 2010). Eight total directions were considered, six based on the ICRP Publication 116 external irradiation geometries (antero-posterior, AP; postero-anterior, PA; left and right lateral, LLAT and RLAT; rotational, ROT; and isotropic, ISO) as well as the top and bottom directions (cranial, CRAN; and caudal, CAUD).

2.1. Literature background

Demonstration of this comprehensive dataset's use was performed through a literature review of five relevant studies of stylized versus voxel phantom comparisons, where the quantification of organ depth differences for these two phantom types would have provided further insight or evidence to their conclusions. In these studies, the greatest differences were seen at lower irradiation energies, where the effects of organ shielding on dosimetry are magnified and where the results of this work are most applicable. Note that these comparative studies involve either the RORNL and UF/NCI phantoms or phantoms of similar lineage, making this depth dataset appropriate for application on their results.

2.1.1. Literature background—RORNL versus UF/NCI phantom comparison study

One comparison study has previously performed a direct comparison of dosimetry results between the two phantom series considered in this work. Within Dewji *et al* (2018), the air submersion exposure scenario was analyzed using the pediatric ages of the RORNL stylized phantom series and the UF/NCI voxel phantom series. An infinite cloud of monoenergetic photon emitters was simulated onto the phantoms, and the resulting photon dose rate coefficients were compared between the series. This air submersion scenario is an apt application of the ISO organ depth dataset generated by the current work.

2.1.2. Literature background—comparison studies with phantoms of similar lineage

In Bellamy *et al* (2016a), their work analyzed the air submersion exposure scenario and compared the photon dose rate coefficients for the RORNL adult stylized phantom and the ICRP adult male voxel phantom—a similar methodology as discussed above for Dewji *et al*. Once again, the dosimetry results of the study are analyzable using the ISO organ depth dataset. In another work, Lee *et al* (2006a) produced organ and effective dose coefficients due to external photons in the six ICRP 116 external irradiation geometries using the original ORNL phantoms and the UF/NCI voxel phantom precursors; considering the close lineage between the ORNL and RORNL phantoms, depth distributions from the current work can be used to help understand these dosimetry differences. As another example, Lee *et al* (Lee and Lee 2004) discussed the impact of unrealistic thyroid positioning in the Medical Internal Radiation Dose (MIRD) phantom. Anatomically, the thyroid is in the lower neck and upper torso region, whereas the location of the thyroid in the MIRD phantom is exclusively in the neck. This same unrealistic thyroid positioning can also be observed in the RORNL phantoms. Their work was therefore to study the effects of thyroid positioning at various vertical positions within the MIRD phantom using different ICRP 116 external irradiation geometries. Lastly, Griffin *et al* (2019) sought to update the phantoms used by the Radiation Effects Research Foundation, which are based on the stylized ORNL phantoms. Within the work, an organ dose comparison of the stylized RORNL series were made to a newly-created phantom series that was based on the UF/NCI series and modified to fit the body parameters of the atomic bomb survivor cohort. Organ depth distributions from the AP direction are thus useful for understanding the dose comparison results for a survivor facing towards the bomb's hypocenter.

3. Methods

The aim of the methodology was to determine the distance from randomly sampled points within an organ to the surface of the body for both stylized and voxel phantoms. A history of 500 000 points were randomly sampled within organs of both phantom series, and the collection of distances calculated to body surface in one of the eight given directions was gathered and binned to create an organ depth distribution. Twenty-four comparable organs between the two series were selected for this work: the adrenals, brain, breasts, colon, extrathoracic region, gall bladder wall, heart wall, kidneys, liver, lungs, muscle, oesophagus, ovaries, pancreas, prostate, salivary glands, small intestine wall, spleen, stomach wall, testes, thymus, thyroid, urinary bladder wall, and uterus. For a given direction, the depth distribution specifies the range of body shielding thickness for an organ against directed external irradiation. For example, the depths for an AP direction are the distances calculated from points within an organ to the front of the body.

Additionally, active marrow (red bone marrow) and shallow marrow (bone surface) organ depth distributions were calculated in this work. To achieve this, distances to the body surface were computed for multiple bone sites in both phantom series. Age-dependent bone marrow distribution fractions in these bone sites were then used to make a weighted-sum estimate of the active and shallow bone marrow depth distributions.

A total of 2496 organ depth comparisons were made from the vast dataset produced by this work, derived from the twenty-four organs and two bone tissues, eight directions, six phantom ages, and two sexes. For reporting conciseness, only those organs with ICRP Publication 103 tissue weighting factors (ICRP 2007) at or above 0.01 will be discussed within the results. The full dataset of organ and bone depth distributions for both phantom series, with 1–2 mm widths of binned depths, can be found in the online supplementary Microsoft Excel workbooks(stacks.iop.org/PMB/65/065007/mmedia).

3.1. Stylized phantom organ depth computation

Although an opportunity exists to use the phantom's complex system of surface equations to determine distances to the body surface, a much easier approach was performed through the use of the particle track output (PTRAC) feature within MCNP6 (Pelowitz 2013). This feature creates a PTRAC file containing a list of user-filtered particle events occurring from the transport within the code. This includes the particle generation, surface crossing, and termination events, which write out the position of each tracked particle during these events. To calculate organ depth, the RORNL phantoms were imported to the MCNP6 code with all materials and cross-sections removed from the model using the 'VOID' card. Particles were generated within an organ through source rejection, where a point was randomly sampled within a bounding box surrounding the phantom; if the selected point was not within the organ, it was rejected from being transported. These particles were started in the opposite direction of organ depth calculation (e.g. AP: particles directed outwards in the PA direction; rotational: any direction in the x-y plane; isotropic: uniform direction generation). The cylindrical geometry of the stylized phantom allows the assumption that in the x-y plane, particles will not leave the body and later re-enter. Thus, the surrounding air was set to an importance weight of zero to kill all particles which reach the body surface in the AP, PA, LLAT, RLAT, and ROT simulations. The straight-line path taken by the particle may have its starting and ending point taken from the PTRAC file and used to calculate the distance from the organ to the body surface. In the CAUD, CRAN, and ISO directions, the particles were allowed to travel to a radius of 200 cm from the origin before they were killed. The PTRAC file then was parsed for surface crossing events to determine the positions where a particle left and possibly re-entered the body in order to determine the total depth. The one exception was for the breasts, where the PTRAC surface crossings were written out for all eight directions. These distances were compiled and binned within a comma-separated value file to create an organ depth distribution.

3.2. Voxel phantom organ depth computation

Code for the voxel phantom organ depth calculation was written in MATLAB, which provides easy handling of matrices. The voxel phantom, in 8-bit unsigned binary format, was read into the code as a large sequence of values, where each value, or tag identifier (ID), represents an organ within the body or the surrounding air. Using the phantom's known matrix dimensions, this sequence was reshaped into a three-dimensional matrix of tag IDs. Out of all voxels matching the organ tag ID, one was randomly sampled, and the distance calculation was started from a random point within the voxel. Using the starting direction of interest, a loop was commenced to sum the distance travelled across the body's voxels, where the user-supplied resolution converts the voxel's dimensions into physical dimensions. While the matrix indices were within the user-supplied matrix dimensions, the distance between the starting point and the next-crossed surface within each voxel was calculated; this allowed the code to keep track of only a local coordinate system for each voxel and the indexed matrix boundaries. The point of intersection from the initial starting point in the voxel to one of the voxel's other surfaces can be found through the parametrized equation given in equation (1):

$$\vec{p}\,(t_{int}) = \overrightarrow{p_0} + \left(\frac{d - \hat{n}\cdot\overrightarrow{p_0}}{\hat{n}\cdot\hat{v}}\right)\hat{v} \tag{1}$$

where $\overrightarrow{p_0}$ is the initial point, $\hat{v}$ is the unit vector for the direction of distance calculation, $\hat{n}$ is the unit normal vector off one of a voxel's surfaces, and d comes from a voxel surface's equation in the form: $\hat{n}\cdot\vec{p} = d$. Of the three possible voxel surfaces the track could cross, the minimum distance from the starting point to a surface was used to determine the next-crossed surface. The point on this surface, $\vec{p}\,(t_{int})$, was translated into the new starting point in the next voxel, and the distance travelled (the magnitude of the added vector) was collected to the total; if the traversed voxel was air, this distance was not collected to the total. On completion, this total distance was stored, and the process was repeated for all sampled points. Subsequently, these distances to the body surface were binned within a comma-separated value file to create an organ depth distribution.

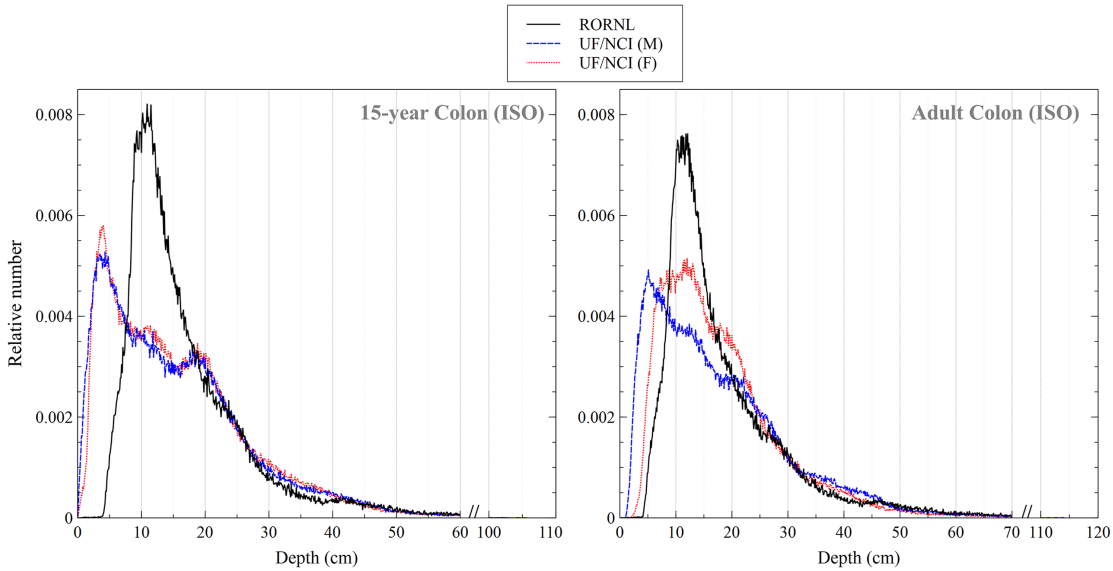

Figure 2. Depth distribution of 500 000 randomly sampled points in the 15-year-old (left) and adult (right) colon in the ISO direction.

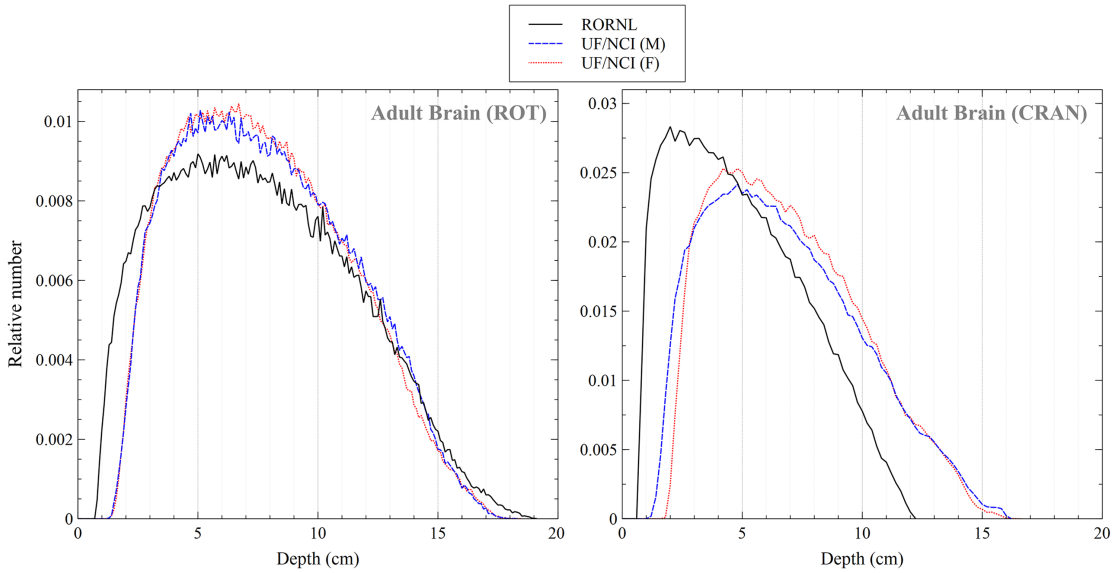

Figure 3. Depth distribution of 500 000 randomly sampled points in the adult brain in the ROT direction (left) and CRAN direction (right).

For validation of this methodology, organ depth distributions were also calculated for the ICRP reference adult male voxel phantom, as previously performed within Annex E of ICRP Publication 110 (ICRP 2009). To our knowledge, this is the only publication of a phantom's organ depth distributions, though there are no data for the rotational or isotropic directions. Excellent agreement was seen in the comparison between the calculated ICRP organ depths and those reported in ICRP 110; these validation results can be found in the online supplementary data.

4. Results

4.1. Organ depth distribution comparisons

In figures 2–6, organ depth distributions calculated within the RORNL phantom series are compared against those calculated within the male and female UF/NCI phantoms. Each distribution is characterized by 1–2 mm widths of binned depths and the relative fraction of the organ within each bin. When comparing the organ depth distributions, those shifted toward the left of the plot are shallower to the body surface than those distributions further to the right.

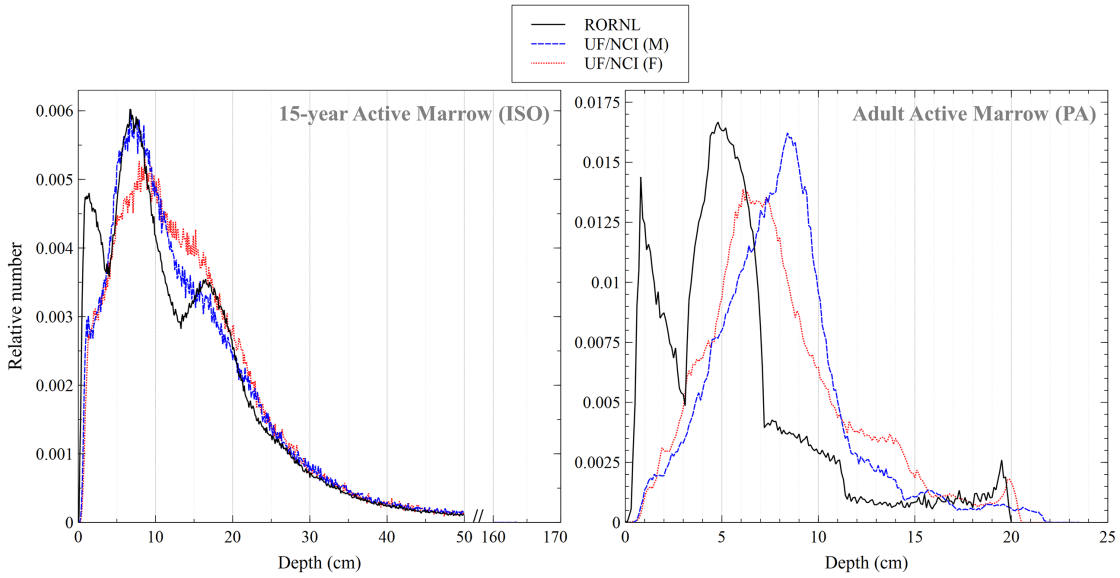

Figure 4. Depth distribution of 500 000 randomly sampled points in the active bone marrow for the 15-year-old in the ISO direction (left) and the adult in the PA direction (right).

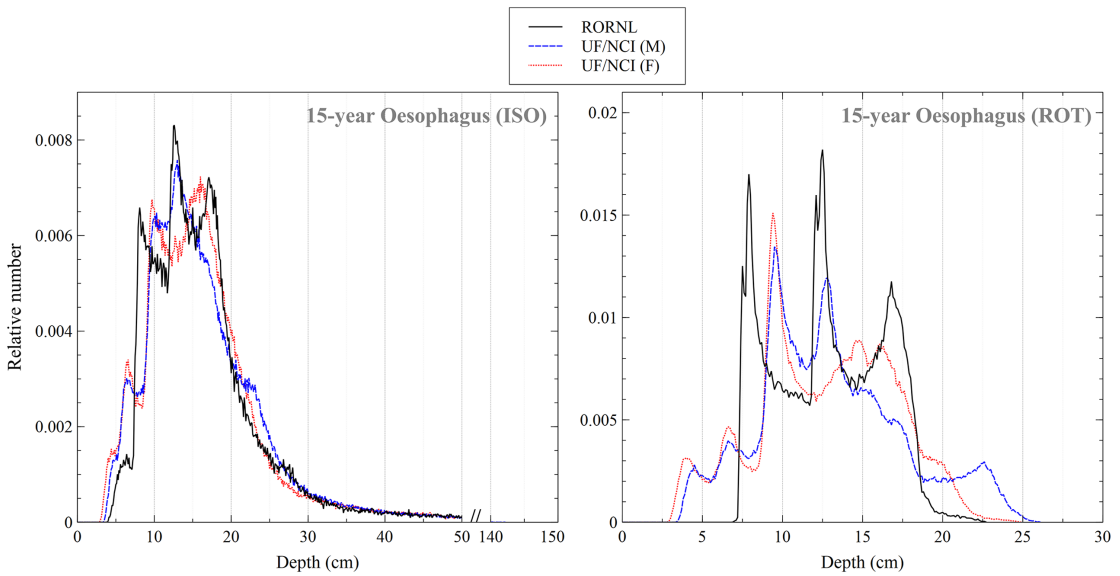

Figure 5. Depth distribution of 500 000 randomly sampled points in the oesophagus for the 15-year-old in the ISO direction (left) and in the ROT direction (right).

4.2. Quantitative data comparisons

Quantitative data descriptors have also been tabulated for the organ depth distributions. Tables 1 and 2 report the minimum, maximum, median, and mean organ depths for the urinary bladder wall and thyroid, respectively. In addition, these two tables also give the standard deviation of the organ depths, as well as the percentage overlap in depth distribution of the UF/NCI series to the RORNL phantom series; for higher overlap percentages, the depth distributions become increasingly congruent, indicating similar organ positioning in the specified direction.

5. Discussion

5.1. Organ depth differences

The methodology presented in this paper provides a novel quantification of the differences in organ positioning between a stylized and voxel phantom series. Specific to the RORNL stylized and UF/NCI voxel phantom series, some interesting trends in organ positioning were noted. From figures 2, 3, and 6, the

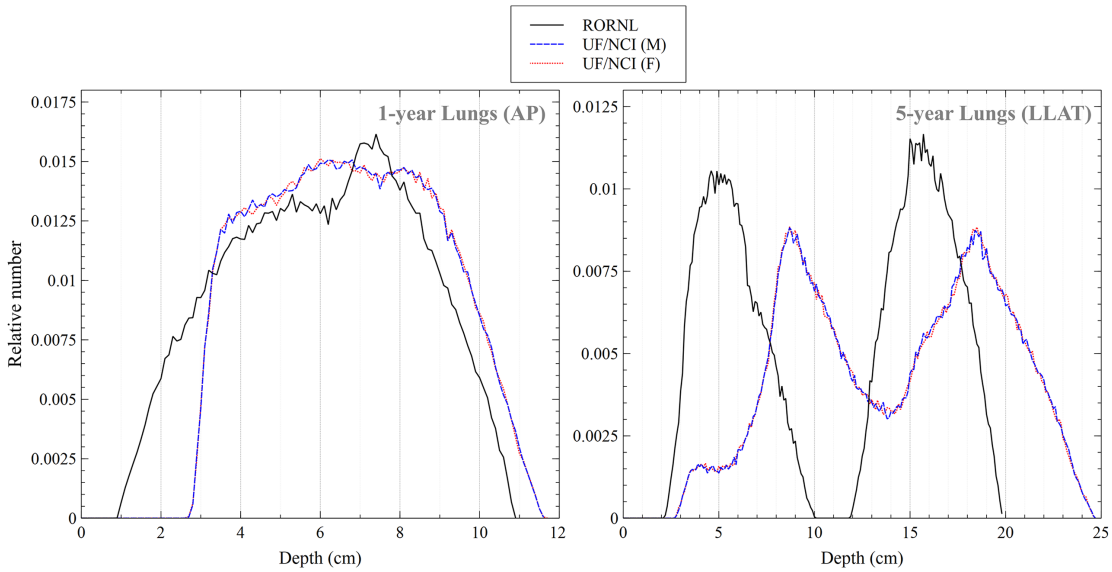

Figure 6. Depth distribution of 500 000 randomly sampled points in the lungs for the 1-year-old in the AP direction (left) and the 5-year-old in the LLAT direction (right).

stylized phantom organ depth distributions are seen to be more regularly distributed than those of the voxel phantom, which have a more asymmetrical shape. This can be attributed to the symmetric nature of the system of equations used to define the stylized phantom; whereas the voxel phantom's lungs have realistic irregularity in organ shape, the stylized phantom defines the lungs as a pair of bisected ellipsoids with a small section removed for the heart's location. Furthermore, it was noted that organ depths in the CAUD direction are generally shallower in the voxel phantom series than in the stylized phantom series. This is believed to be due to the definition of the legs in the stylized phantoms, where the legs are pressed together and slope inwards, as seen in figure 1; in the voxel phantom series, the legs are naturally separated, providing less shielding from the CAUD direction. Although these two series are defined through very different means, they both show a similar characteristic: the LLAT and RLAT organ depth distributions are typically similar when compared to each other. This indicates that both series are demonstrating the bilateral symmetry of the human body.

In figure 6, it can be acknowledged that the male and female UF/NCI phantoms have an identical lung depth distribution. According to their original publication, the UF/NCI phantoms share the same body between sexes at ages 10 and below, apart from the sex-specific organs (e.g. prostate, uterus, etc.); this is reflected within the dataset, with identical depth distributions seen between sexes for the shared organs at ages 10 and below. The one exception is in the urinary bladder wall where, beginning at age 5, the female bladder has been positioned closer to the front of the body to accommodate the placement of the uterus, as seen in table 1.

Across all ages, the organ positioning generally grows deeper with increasing age. In the RORNL series, the mean organ depths monotonically increase with increasing age for 198 organ-direction combinations out of 208 total. In the UF/NCI series, this is also true for 245 organ-direction combinations out of 384 total. In table 1, one can see the trend of increasing mean depth of the urinary bladder wall in the LLAT direction. However, in the UF/NCI series the thyroid shows the opposite trend; as seen in table 2, the UF/NCI thyroid becomes positioned more forwardly within the neck with increasing age from 1 to 10 years, with a decreasing minimum depth and decreasing mean depth. The RORNL series does not show this trend, however.

5.2. Retrospective application: literature review

5.2.1. Literature review: RORNL versus UF/NCI comparison study

From the results of Dewji *et al* (2018), an up to 35% increase in colon dose was evaluated from the switch to the UF/NCI voxel series from the RORNL stylized series. As seen in figure 2, the 15-year-old UF/NCI colon depth distribution is much shallower to the body surface from an isotropic irradiation scenario than in the RORNL series. Additionally, a 10% decrease in active marrow dose was found in the switch from the 15-year-old stylized to voxel phantom. Though this is likely compounded by their use of two separate marrow distributions with the two series, figure 4 shows that the active marrow distribution is found to be slightly deeper within the UF/NCI phantom series. Lastly, this publication showed up to a 40% expected

Table 1. Compiled data for the 1-, 5-, and 10-year-old urinary bladder wall in the AP, LLAT, and PA directions showing the minimum, maximum, median, and mean with standard deviation. Additionally, the UF/NCI to RORNL depth overlap percentage is shown.

View	Type	Sex	Age	Min (cm)	Max (cm)	Median (cm)	Mean (cm)	Standard Deviation (cm)	Overlap (%)
AP	RORNL		1	0.7	5.5	3.0	3.02	1.31	—
			5	0.8	6.3	3.4	3.46	1.53	—
			10	0.9	6.9	3.8	3.83	1.70	—
	UF/NCI	F	1	3.2	6.0	4.8	4.81	0.66	39.4
			5	0.4	6.3	2.8	3.00	1.63	87.3
			10	2.9	8.5	5.0	5.16	1.46	63.1
		M	1	3.3	6.4	5.3	5.19	0.79	37.5
			5	2.0	7.8	4.8	4.87	1.67	69.8
			10	3.7	9.8	6.2	6.30	1.56	48.4
LLAT	RORNL		1	3.5	10.3	7.3	7.21	1.77	—
			5	4.6	13.4	9.4	9.34	2.32	—
			10	5.6	16.2	11.4	11.28	2.78	—
	UF/NCI	F	1	6.5	12.9	9.9	9.80	1.55	50.3
			5	6.6	17.3	11.7	11.98	2.80	60.5
			10	8.8	18.9	13.9	13.84	2.35	66.1
		M	1	6.5	12.8	9.6	9.56	1.55	56.0
			5	7.6	17.0	11.9	12.04	2.41	63.2
			10	8.4	17.3	13.2	12.84	2.40	75.6
PA	RORNL		1		12.4	9.9	9.90	1.32	—
			5	8.8	14.3	11.4	11.47	1.53	—
			10	10.0	16.0	12.9	12.90	1.70	—
	UF/NCI	F	1	5.1	9.1	7.3	7.21	0.99	28.8
			5	6.4	12.2	9.0	9.09	1.67	52.6
			10	6.4	13.0	9.3	9.45	1.83	39.3
		M	1	5.0	9.1	6.9	6.96	1.02	26.6
			5	4.6	10.4	6.6	6.94	1.62	17.9
			10	5.2	11.2	8.3	8.27	1.58	17.0

increase in oesophagus dose for 100 keV photons in the switch to voxel phantom use in the 15-year-old model; within their discussion, they suggest that this is due to shallower positioning in the body. In figure 5, the isotropic distances in the 15-year-old oesophagus seem to show similar depth distributions in both series. However, in the rotational view, it can be noted that a significant portion of the UF/NCI oesophagus is quite shallow (depths starting at around 2 cm) while the entirety of the RORNL organ is more shielded (depths starting at around 7 cm). Considering the mean free path of around 6 cm for 100 keV photons in tissue, this difference in shielding for a portion of the oesophagus likely created the significant dose difference reported in the publication.

5.2.2. Literature review: studies with phantoms of similar lineage

From the results of Bellamy *et al* (2016a), the colon dose was reported to be 26% higher in the ICRP adult voxel phantom than in the RORNL stylized phantom for 100 keV photons, as was also noted for the pediatric ages in Dewji *et al* In figure 2, the ISO organ depth distributions of the UF/NCI and RORN L adult male colons make evident that a significant portion of the colon in the RORNL stylized phantom is positioned deeper than the colon in the UF/NCI voxel phantom. Conversely, the brain dose was reported 12% lower in the ICRP voxel phantom. As shown in figure 3, the ROT and CRAN organ depth distributions of the adult brain show the RORNL phantom is indeed slightly shallower than its voxel phantom counterpart.

It was found in Lee *et al* (2006a) that the urinary bladder wall of the UF/NCI voxel phantom series received up to 50% more dose than the ORNL phantom series from the PA exposure scenario, which was attributed to the thicker abdominal tissues in the ORNL phantoms and a more centrally-located urinary bladder in the voxel phantoms. As seen in table 1, the voxel series urinary bladder wall of ages 1 to 10 is indeed positioned around 3–4 cm closer to the back of the phantom and 0–2 cm further from the front of the body. Another major result mentioned in the discussion of Lee *et al* was one that described the vast difference seen in the lung dose coefficients between the 5-year-old phantoms—a greater than 35% dose decrease in voxel phantom lung dose was reported in the lateral geometries. As seen in figure 6, the 5-year-old stylized phantom lungs are indeed much shallower in the LLAT directions; supplementary data also show that the stylized lungs are much shallower in the RLAT direction as well. This can be attributed, as mentioned in

Table 2. Compiled data for the 1-, 5-, and 10-year-old thyroid in the AP, CRAN, and LLAT directions showing the minimum, maximum, median, and mean with standard deviation. Additionally, the UF/NCI to RORNL depth overlap percentage is shown.

View	Type	Sex	Age	Min (cm)	Max (cm)	Median (cm)	Mean (cm)	Standard Deviation (cm)	Overlap (%)
AP	RORNL		1	1.4	7.1	1.8	1.90	0.81	—
			5	1.7	8.6	2.2	2.36	0.94	—
			10	1.3	8.9	2.0	2.06	0.88	—
	UF/NCI	F	1	1.7	5.8	2.7	2.80	0.60	11.7
			5	0.8	2.4	1.4	1.45	0.35	22.6
			10	0.1	3.1	1.3	1.37	0.56	47.4
		M	1	1.7	5.6	2.7	2.80	0.60	11.5
			5	0.8	2.4	1.4	1.45	0.35	22.6
			10	0.1	3.1	1.3	1.37	0.57	47.1
CRAN	RORNL		1	15.6	17.8	16.6	16.63	0.61	—
			5	17.4	20.2	18.8	18.80	0.76	—
			10	18.0	21.6	19.8	19.77	0.98	—
	UF/NCI	F	1	16.6	18.4	17.6	17.54	0.42	43.2
			5	19.6	22.2	20.8	20.74	0.52	13.2
			10	19.0	24.0	21.8	21.80	0.90	33.1
		M	1	16.6	18.4	17.6	17.54	0.42	43.3
			5	19.6	22.2	20.8	20.74	0.52	13.2
			10	19.0	24.0	21.8	21.80	0.90	33.0
LLAT	RORNL		1	2.4	9.7	3.0	3.30	1.06	—
			5	2.7	12.5	3.5	3.81	1.37	—
			10	2.4	15.4	3.5	3.89	1.59	—
	UF/NCI	F	1	2.3	8.2	5.0	5.04	1.26	25.8
			5	1.4	9.4	3.9	4.08	1.60	52.1
			10	0.1	13.9	5.4	5.74	3.23	34.8
		M	1	2.3	8.2	5.0	5.04	1.26	25.8
			5	1.4	9.4	3.9	4.07	1.60	52.1
			10	0.1	14.0	5.4	5.74	3.23	34.8

another publication by Lee *et al* (2006b), to the incorporation of the arms into the torso of the stylized phantom, which leads to large differences in the amount of body shielding from lateral directions.

In Lee and Lee (2004), the thyroid absorbed dose within the MIRD phantom was shown to decrease by as much as 60% in the RLAT and LLAT directions when the thyroid was relocated into a realistic vertical position within the torso. As seen in table 2 in the CRAN direction, the vertical thyroid positioning within the RORNL series is also relatively higher than is seen in the UF/NCI series, as the entire thyroid has been placed within the neck region. Looking in the LLAT direction, differences in depth are notable when comparing the RORNL series to the UF/NCI series; from this, one might expect the thyroid dose to be significantly different for the stylized RORNL series and a voxel phantom series. Indeed, as seen in figure 2 of Lee *et al* (2006a), the expected thyroid dose from an LLAT directed broad beam is considerably lower in their voxel phantom series than in the ORNL stylized series.

Lastly, from Griffin *et al* (2019), one finding on photon dose differences showed that the 1-year old lungs had dose estimated around 18% higher in the RORNL stylized series than in their voxel phantom series from the AP direction. As seen in figure 6, the 1-year RORNL stylized phantom lungs are indeed located in a shallower AP position as compared to the UF/NCI series.

5.3. Future applications and study limitations

The results described within this work help explain previous findings from multiple authors; these results, along with the underlying methodologies, can be extended to many future applications as well. One example is the upcoming work performed by the ICRP Committee 2's Task Group 90—age-dependent dose conversion coefficients for external exposures to environmental sources. Historically, the Environmental Protection Agency has addressed the community's need for these dose coefficients through published reports Federal Guidance Report (FGR) 12 of 1993 and FGR 15 of 2018 (Eckerman and Ryman 1993, Bellamy *et al* 2018). The proposed update is in the utilized phantom for the dose calculations: FGR uses the stylized ORNL phantom series while Task Group 90 intends to provide dose coefficients using the ICRP pediatric and adult voxel phantoms. In this manner, quantitative data on organ depth differences would prove useful for interpreting dose differences from these external exposures. The methodology of this work may prove useful for applications in phantom development as well; one example is in the body-size varied UF/NCI phantom

library. As detailed within separate work (Geyer *et al* 2014), the UF/NCI library of phantoms was created by adjusting the previous reference-size phantoms to match the height and weight of individuals of varying body mass index. Although the outer body contour was adjusted to match each individual's height and weight, and the organ masses were matched to reference values, organ position was unable to be considered. It may therefore be of value to use the methodology described in this work to adjust the organ positioning for phantoms of the same height such that there is a systematic increase in organ depth with increasing weight for relevant organs in the torso or other parts of the body. Future work may also use a re-tooled version of this methodology to evaluate the intra-organ distances within stylized and voxel phantom series to determine the impact this type of switch may have in nuclear medicine dosimetry.

From the thousands of organ depth distributions evaluated from this work, results and comparisons are available for many different applications. However, the methodologies used to create these depths have limited the power behind the dataset. For instance, the geometrical organ depth does not provide a complete picture on dose differences for regions of the body with strong heterogeneity, such as the region around the lungs. Under these circumstances, where water-equivalent thickness might instead provide a more appropriate evaluator, caution should be exercised in their application. Additionally, the organ depths from this work were calculated from straight-line paths from randomly sampled points in the organ through the body tissues. These measurements only account for the body shielding from unattenuated radiations; therefore, these organ depths may not be representative enough of the actual photon path to justify dosimetric differences found in certain applications. For example, the RORNL phantom series has the arm bones incorporated within the torso of the body, which can act as a stronger scatter source to organs such as the liver in an AP or PA scenario when compared to the arm-separated UF/NCI series. As another example, the calculated isotropic body depths are in all directions evenly; this depth calculation is biased towards treating all directions equally, which may also be misrepresentative of the actual photon path. In a realistic isotropic source, such as air submersion, an almost insignificant amount of dose to the brain or other head organs would originate from lower-energy particles travelling through the bottom of the body. In this situation, the rotational depth would provide better comparisons for head shielding, as was previously shown for the oesophagus comparison in section 4.2. An isotropic organ depth distribution would be more helpful for organs that are closer to the abdominal region. Lastly, one may note that the active bone marrow and shallow bone marrow comparisons are only useful for the assumed marrow distributions used within this study. As shown in the literature review, even within the same study, different marrow distributions have been used with different phantom series. For this reason, the individual bone site depth distributions were kept and are given in the supplementary data for those wishing to impose different marrow distributions, such as those published with the original ORNL stylized phantom (Cristy and Eckerman 1987).

6. Conclusions

The purpose of this work was to fill a knowledge gap in external irradiation dosimetry: a quantification of body shielding differences between stylized and voxel phantoms. The differences found when comparing different generations of external dose coefficients may often be attributable to this information. Methodology was devised to compute the distance from the body surface to any organ from any directional exposure detailed within ICRP Publication 116, as well as the CAUD and CRAN directions, for both phantom series. Similarities between the two series were seen, such as their bilateral human symmetry when comparing LLAT and RLAT depths. On the other hand, general differences were observed between the stylized and voxel phantoms, such as the stylized phantom's greater body shielding from the CAUD irradiation direction. Demonstration of this dataset's use was performed through a literature review of relevant stylized versus voxel phantom comparison works, which helped provide evidence to the dosimetry results found therein. The entire dataset, along with validation results and individual bone site depths, can be found online in the supplementary data.

Acknowledgments

This research was funded by the intramural research program of the National Institutes of Health, National Cancer Institute, Division of Cancer Epidemiology and Genetics. The views of the authors do not necessarily reflect those of the government. Certain commercially available software is identified in this manuscript to foster understanding and should not be construed as a recommendation. This work utilized the computational resources of the NIH High-Performance Computing Biowulf cluster (http://hpc.nih.gov).

ORCID iDs

Keith T Griffin https://orcid.org/0000-0002-9628-3791
Shaheen A Dewji https://orcid.org/0000-0002-3699-5877

References

Bellamy M *et al* 2018 *External Exposure to Radionuclides in Air, Water, and Soil* (Washington, DC: US Environmental Protection Agency)
Bellamy M B, Hiller M M, Dewji S A, Veinot K G, Leggett R W, Eckerman K F, Easterly C E and Hertel N E 2016a Comparison of monoenergetic photon organ dose rate coefficients for stylized and voxel phantoms submerged in air *Radiat. Prot. Dosim.* **172** 367–74
Bellamy M B, Veinot K G, Hiller M M, Dewji S A, Eckerman K F, Easterly C E, Hertel N E and Leggett R W 2016b Effective dose rate coefficients for immersions in radioactive air and water *Radiat. Prot. Dosim.* **174** 275–286
Cristy M and Eckerman K F 1987 *Specific Absorbed Fractions of Energy at Various Ages from Internal Photon Sources* (Oak Ridge, TN: Oak Ridge National Laboratory)
Dewji S, Bellamy M, Hertel N, Leggett R, Sherbini S, Saba M and Eckerman K 2015b Estimated dose rates to members of the public from external exposure to patients with ^{131} I thyroid treatment: external dose rates from ^{131} I patients *Med. Phys.* **42** 1851–7
Dewji S, Hiller M, Bellamy M, Akkurt H, Wiarda D, Kora G and Eckerman K 2017 NUREG/CR-7243, PIMAL: Phantom with Moving Arms and Legs Version 4.1.0. 93
Dewji S A, Bales K, Griffin K, Lee C and Hiller M 2018 Age-dependent comparison of monoenergetic photon organ and effective dose coefficients for pediatric stylized and voxel phantoms submerged in air *Phys. Med. Biol.* **63** 175019
Dewji S A, Bellamy M, Hertel N, Leggett R, Sherbini S, Saba M and Eckerman K 2015a Assessment of the point-source method for estimating dose rates to members of the public from exposure to patients with 131I thyroid treatment *Health Phys.* **109** 233–41
Eckerman K and Ryman J 1993 *External Exposure to Radionuclides in Air, Water, and Soil* (Washington, DC: US Environmental Protection Agency)
Geyer A M, O'Reilly S, Lee C, Long D J and Bolch W E 2014 The UF/NCI family of hybrid computational phantoms representing the current US population of male and female children, adolescents, and adults—application to CT dosimetry *Phys. Med. Biol.* **59** 5225–42
Griffin K, Paulbeck C, Bolch W, Cullings H, Egbert S, Funamoto S, Sato T, Endo A, Hertel N and Lee C 2019 Dosimetric impact of a new computational voxel phantom series for the japanese atomic bomb survivors: children and adults *Radiat. Res.* **191** 369–79
Han E Y, Bolch W E and Eckerman K F 2006 Revisions to the ORNL series of adult and pediatric computational phantoms for use with the MIRD schema *Health Phys.* **90** 337–56
Hiller M and Dewji S A 2017 Comparison of monoenergetic photon organ dose rate coefficients for the female stylized and voxel phantoms submerged in air *Radiat. Prot. Dosim.* **175** 336–43
ICRP 2007 The 2007 recommendations of the international commission on radiological protection *ICRP Publ. 103 Ann. ICRP* **37** 1–332
ICRP 2009 Adult reference computational phantoms *ICRP Publ. 110 Ann. ICRP* **39** 1–166
ICRP 2010 Conversion coefficients for radiological protection quantities for external radiation exposures *ICRP Publ. 116 Ann. ICRP* **40** 1–258
Lee C, Lee C and Bolch W E 2006a Age-dependent organ and effective dose coefficients for external photons: a comparison of stylized and voxel-based paediatric phantoms *Phys. Med. Biol.* **51** 4663–88
Lee C, Lee C and Lee J-K 2006b On the need to revise the arm structure in stylized anthropomorphic phantoms in lateral photon irradiation geometry *Phys. Med. Biol.* **51** N393
Lee C and Lee J 2004 The effect of unrealistic thyroid vertical position on thyroid dose in the MIRD phantom *Med. Phys.* **31** 2038–41
Lee C and Lee J K 2007 Applicability of dose conversion coefficients of ICRP 74 to Asian adult males: Monte Carlo simulation study *Appl. Radiat. Isot.* **65** 593–8
Lee C, Lodwick D and Bolch W E 2007 NURBS-based 3D anthropomorphic computational phantoms *Radiat. Prot. Dosim.* **127** 227–32
Lee C, Lodwick D, Hurtado J, Pafundi D, Williams J L and Bolch W E 2010 The UF family of reference hybrid phantoms for computational radiation dosimetry *Phys. Med. Biol.* **55** 339–63
Liu H, Gu J, Caracappa P F and Xu X G 2010 Comparison of two types of adult phantoms in terms of organ doses from diagnostic CT procedures *Phys. Med. Biol.* **3** 1441–51
Pelowitz D B 2013 MCNP6 User's Manual Version 1.0
Roesch W C 1987 *US-Japan Joint Reassessment of Atomic Bomb Dosimetry in Hiroshima and Nagasaki: Final Report* (Hiroshima, Japan: Radiation Effects Research Foundation)
Veinot K G, Eckerman K F, Bellamy M B, Hiller M M, Dewji S A, Easterly C E, Hertel N E and Manger R 2017 Effective dose rate coefficients for exposure to contaminated soil *Radiat. Environ. Biophys.* **56** 255–67
Xie T, Akhavanallaf A and Zaidi H 2019 Construction of patient-specific computational models for organ dose estimation in radiological imaging *Med. Phys.* **46** 2403–11
Xie T, Poletti P-A, Platon A, Becker C D and Zaidi H 2018 Assessment of CT dose to the fetus and pregnant female patient using patient-specific computational models *Eur. Radiol.* **28** 1054–65
Xie T and Zaidi H 2019 Estimation of the radiation dose in pregnancy: an automated patient-specific model using convolutional neural networks *Eur. Radiol.* **29** 6805–15
Xu X G 2014 An exponential growth of computational phantom research in radiation protection, imaging, and radiotherapy: a review of the fifty-year history *Phys. Med. Biol.* **59** R233-302
Yoriyaz H, Dos Santos A, Stabin M G and Cabezas R 2000 Absorbed fractions in a voxel-based phantom calculated with the MCNP-4B code *Med. Phys.* **27** 1555–62
Young R W and Kerr G 2005 *Reassessment of the Atomic Bomb Radiation Dosimetry for Hiroshima and Nagasaki – Dosimetry System 2002* (Hiroshima, Japan: Radiation Effects Research Foundation)
Zaidi H and Xu X G 2007 Computational anthropomorphic models of the human anatomy: the path to realistic Monte Carlo modeling in radiological sciences *Annu. Rev. Biomed. Eng.* **9** 471–500